Beyond and beneath displacement time series: towards InSAR-based early warnings and deformation analysis of the Achoma landslide, Peru

Benedetta Dini[1,2], Pascal Lacroix[2], Marie-Pierre Doin[2]

[1]School of Geography, Earth and Environmental Sciences, University of Birmingham, Birmingham, UK

[2]ISTerre, Université Grenoble-Alpes, Grenoble, France

Corresponding author:

Benedetta Dini, School of Geography, Earth and Environmental Sciences, University of Birmingham, Birmingham, UK

Formerly at: ISTerre, Université Grenoble-Alpes, Grenoble, France

orcid number: 0000-0002-1578-7294

Email address: b.dini@bham.ac.uk

Abstract

Detecting precursors to slope destabilisation with sufficient lead time and accuracy remains a challenging and unresolved issue in landslide hazard assessment and prediction. This is key, as catastrophic landslides often go unnoticed until immediately before or after failure, limiting opportunities for intervention. While in situ methods offer high accuracy at point locations, they are costly and require prior knowledge of instability. Satellite-based synthetic aperture radar differential interferometry (InSAR) has shown promise in identifying unknown landslides over large areas and has been proposed as a potentially useful tool for failure prediction. Typically valued for retrieving displacement time series, InSAR time series reliability depends heavily on successful interferogram unwrapping, which often leads to severe underestimations over landslides. Here, we analyse the deformation process of the Achoma landslide in Peru and demonstrate that the InSAR signal contains precursors based on alternative markers, even without displacement time series. Interferometric coherence shows the formation of gravitational structures up to five years before failure, as well as a critical shift in landslide behaviour three months prior to failure. Additionally, a marker based on the wrapped phase reveals and quantifies alternating periods of quiescence and motion, the latter becoming more frequent in the two years before failure. Our findings highlight the potential to use alternative InSAR signal markers to observe the deformation process and

progressive failure leading up to the event, and to detect landslide precursors across extensive areas, providing valuable lead time for intervention and disaster prevention.

Keywords:
InSAR - Landslide precursors – Incipient slope destabilisation - Early warning indicators Progressive failure – Landslide dynamics – Interferometric coherence - Interferometric wrapped phase

1. Introduction

Landslides pose a global threat, causing more than 4000 fatalities annually (Petley 2012) including more than 4,000 resulting from non-seismic triggers (Froude and Petley 2018). Beyond the human toll, landslides lead to substantial social and economic consequences in both developing and developed countries. Despite advances in hazard assessment, predicting when and where potentially unstable hillslopes will fail catastrophically remains a major challenge. This highlights the critical importance of early identification of destabilizing slopes and the detection of accelerating phases, which are key to improving prediction and preparedness (e.g.,Carlà et al., 2017; Roy et al., 2022; Strząbała et al., 2024; Valletta et al., 2022).

While there are documented instances of successful predictions and early warnings using in-situ methods (e.g., Badoux et al., 2009; Fan et al., 2019; Loew et al., 2017), two main challenges persist: cost and feasibility of monitoring all known unstable slopes, and the limited pre-existing knowledge of instability, which often leads to landslides remaining unnoticed until severe acceleration or catastrophic failure occurs (Guzzetti, 2021; Palmer, 2017), causing significant delays in the installation of monitoring systems (e.g., Fiolleau et al., 2020).

The advent and use of satellite-based technologies, particularly satellite-based synthetic aperture radar differential interferometry (InSAR), have significantly improved landslide identification capabilities (e.g. Strząbała et al., 2024). Observations can be made more cost-effectively due to the increasing availability, frequency, and reliability of acquisitions, whilst the large coverage (Costantini et al., 2021; Lacroix et al., 2022a; Wasowski and Bovenga, 2022) may allow for the identification of previously unknown unstable slopes at large scales (Dini et

al., 2019, 2020). This enhances the possibility of implementing timely and targeted monitoring before disasters occur. Identifying destabilising slopes from satellite data is crucial also for landslides in remote locations, which are challenging to spot and monitor in-situ, yet can generate far-reaching hazard cascades (Cook et al., 2021). With increasing temporal sampling of new generation satellites (e.g. Sentinel-1) and the potential for sub-centimetre displacement accuracy in favourable conditions (Ferretti et al., 2011; Liu et al., 2013; Wasowski and Bovenga, 2014), the use of InSAR has become widespread for generating landslide displacements time series based on small baseline subset (Berardino et al., 2002) (SBAS) or permanent scatterers (Ferretti et al., 2005, 2001) (PS) algorithms, and variations of these. In a few cases, retrospective retrieval of time series revealed acceleration patterns leading to failure, highlighting potential for accurate prediction of failure timing (Carlà et al., 2019; Intrieri et al., 2018).

However, despite InSAR's remarkable potential for geohazard observation, the universal reliability of InSAR displacement time series is not guaranteed, due to significant challenges related to the nature of the phenomena and data processing limitations. We highlight here only the limitations relevant to this work. For a more exhaustive account we refer to Lacroix et al. (2021) and references therein.

Small to medium-size landslides (a few tens to a few hundred m along-scarp length) in many cases only cover a relatively small number of SAR pixels on the ground (e.g., for the pixel size of Sentinel-1, 2.3 m by 14.1 m), making signal detection challenging. Moreover, not all landslides are expected to exhibit measurable precursory deformation prior to failure. Rapid, shallow landslides in loose materials may fail abruptly with no significant precursors. Larger landslides (several hundred m along-scarp length) may exhibit displacements only on isolated sectors at different times. Additionally, landslides often present strong spatial gradients and sharp displacement edges (e.g. Cheaib et al., 2022) that make phase unwrapping problematic due to phase aliasing (Manconi, 2021; Strząbała et al., 2024). Finally, landslides often display non-linear behaviour in time, with phases of accelerations interspersed with periods of quiescence. This is unfavourable for InSAR time series based on SBAS or PS approaches (e.g. (Handwerger et al., 2025), particularly when temporal sampling is affected by missing acquisitions or unusable images (e.g., snow cover, seasonal landcover changes). When a slope transitions from no displacement to fast reactivation, with displacements exceeding a threshold (commonly ¼ of the wavelength)

between two acquisitions and/or between adjacent pixels when gradients are strong, phase aliasing and decorrelation occur. The lack of phase continuity makes it difficult to accurately reconstruct the continuous phase signal from the wrapped phase measurements. As conventional processing methods for generating displacement time series rely on phase unwrapping, they are particularly susceptible to phase aliasing(Manconi, 2021). Moreover, as interferometric coherence decreases, unwrapping over critical areas might not be performed when processing large areas due to the cutoff imposed using coherence thresholds. This leads to the loss of any true deformation signal potentially contained in low- (or lower-) coherence interferograms. In essence, the success on landslide of common InSAR approaches heavily relies on the existence of many conditions favourable to processing. Without individual interferogram inspection, a time-consuming task, an InSAR displacement time series might seem accurate and plausible, yet it could significantly underestimate the true displacements and obscure crucial acceleration phases and/or their magnitude (Dini et al., 2020; Jacquemart and Tiampo, 2021). Consequently, there is a high potential for misinterpreting the ongoing processes driving instability and assessing the hazard level.

In response to the challenges associated with InSAR, some authors focused on the analysis of high temporal frequency optical images (e.g., Sentinel-2, PlanetLab) to derive time series of displacements (Lacroix et al., 2018, 2023), or changes in vegetation cover caused by landslides with NDVI from Sentinel-2 acquisitions (Yang et al., 2019). However, optical data are constrained by cloud coverage and have limited sensitivity to smaller displacements that might occur over longer time frames leading up to failure. Others have successfully retrieved acceleration phases through image correlation of SAR images (Li et al., 2020), but this method is also limited to the observation of relatively large displacements (greater than 1/10 of the pixel size), thus more suitable to cover the final weeks to months of an accelerating phase. Consequently, alternative and/or complementary InSAR-based techniques must be developed to improve our ability to observe landslide precursors beyond what is possible using only methods reliant on phase unwrapping. Jacquemart et al. (2021) focused on InSAR coherence, showing a temporal decrease of coherence roughly 5 months prior to the Mudcreek landslide failure. To our knowledge this is the only study on this topic, highlighting the need for more case-studies and in-depth understanding of landslide behaviours associated with this type of signal. Since rapid, shallow landslides may fail without measurable precursors, coherence-based approaches are likely most effective for

larger, slower, or more complex landslides where deformation evolves progressively over time.

Our work introduces a novel methodology for extracting landslide precursors that bypasses traditional time series generation. Instead, we integrate information on incipient and ongoing instability using interferometric coherence and wrapped phase. This approach is particularly valuable when full displacement time series are unavailable or unreliable. By addressing the limitations of conventional methods, we offer an alternative perspective on landslide precursor identification from space. This paper explores two critical questions: Can interferometric coherence serve as an effective precursor for identifying critical landslide phases and incipient instability in both time and space? And can indicators based on the wrapped phase provide insights into criticality of landslide behaviour, in the absence of a reliable displacement time series?

To illustrate our methodology, we present a case study on the Achoma landslide in the Colca Valley, Peru. This landslide exemplifies an instability that remained unnoticed on the ground until shortly before catastrophic failure, while retrospective analysis using optical satellite images detected signals three months before the event (Lacroix et al., 2023). Although our analysis is retrospective, the signals identified represent genuine precursory indicators detectable in the InSAR data before failure. Remarkably, our results show that signs of destabilisation were detectable five years prior to failure. The subsequent sections of this paper detail the methods we employed, including topographic error correction, coherence loss analysis, and the extraction of wrapped phase temporal behaviour. Finally, we present our results and discuss their significance, highlighting the potential integration of our approach with traditional methods.

2. Study area

The deeply incised Colca Valley is located in southern Peru. On its terraces, it hosts several settlements, largely supported by extensive agriculture. The valley is located between volcanic massifs to the north and south (Zerathe et al., 2016), and is characterised by sequences of ignimbrites and pyroclastic deposits. The valley's geomorphology has been shaped by debris avalanches from valley flank collapses followed by landslide dam

breakouts(Thouret et al., 2007), with one such event forming a paleolake and depositing thick lacustrine deposits (Lacroix et al., 2015; Zerathe et al., 2016).

Seismicity in the region has distinct sources (Lacroix et al., 2023 and references therein; Zerathe et al., 2016), from relatively low magnitude (Mw <3) seismic events originating in the volcanic area approximately 15-20 km to the southwest, to larger magnitude earthquakes associated with regional tectonic faults (Mw <7) or Mw 8 events with origin in the subduction zone roughly 100 km to the west.

The area experiences a seasonal climate pattern, with most of the rainfall falling between December and April (Lacroix et al., 2015), followed by a dry season. Annual rainfall amounts range between 350 and 600 mm, with daily cumulative precipitation rarely exceeding 25 mm. Numerous large landslides dot the Colca valley (Pham et al., 2018), often showing retrogressive failure in the lacustrine deposits (Zerathe et al., 2016) and responding to different trigger mechanisms (Bontemps et al., 2020; Lacroix et al., 2015, 2023). Persistent uncertainties surround the factors controlling their evolution into slow or rapid landslides (Zerathe et al., 2016), making the evaluation of their hazard potential difficult. Other landslides in the valley that have been long creeping have been instrumented for years (Bontemps et al., 2020; Lacroix et al., 2014, 2015; Palmer, 2017), providing valuable insights into landslide dynamics and responses to seismic and climatic triggers.

The Achoma landslide, failed catastrophically on 18th June 2020, unnoticed for a long time until cracks were reported by locals in May 2020 (Dini et al., 2022; Lacroix et al., 2023), only one month prior to failure. It is a large and deep-seated landslide that spans approximately 800 m in width along its scarp and extends 500 m downslope to the Colca River, covering an area of about 0.4 km^2 (Figure 1). The headscarp rises approximately 100 m high (Lacroix et al., 2023), with estimated rupture surface depth averaging 50 m. The landslide volume is thus estimated at around 20 x 10^6 m^3.

The failure occurred during the dry season, following cumulative rainfall of 600 mm during the preceding wet season. Earlier findings indicated the landslide gradually accelerated three months before its failure, initiating during the rainy season (Lacroix et al., 2023), suggesting rainfall may have played a crucial role in the transition from slow to rapid movement. The site

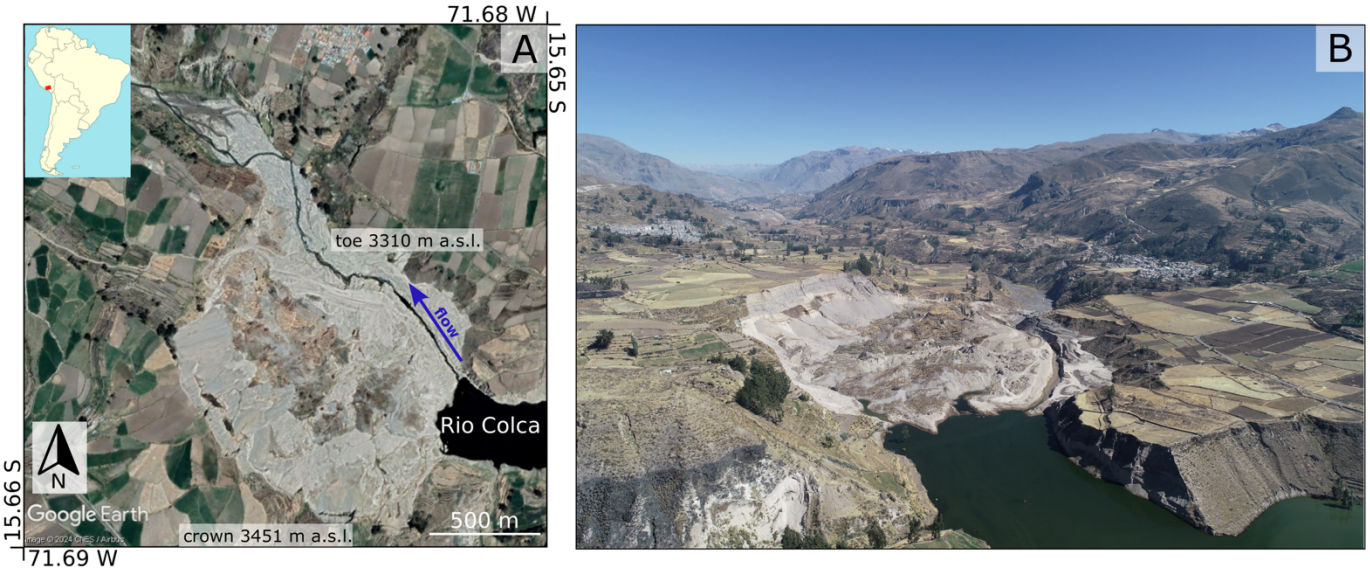

Figure 1. A) Study area, Achoma landslide post failure (©GoogleEarth Image, CNES/Airbus 1/11/2020). Red rectangle in top left inset shows footprint of Sentinel 1 images (relative orbit number 47). B) Drone image of the landslide, looking northwest. Credits: Ingemmet.

has experienced seismic activity during the observation period, with the largest earthquake recorded on 15th August 2016, measuring Mw 5.5 (Bontemps et al., 2020).

3. Methods and data

3.1. Raw interferograms

We generated 514 Sentinel-1 wrapped interferograms from 114 satellite acquisitions of ascending track with relative orbit number 47, covering the period between 30th April 2015 and 20th June 2020 (the rupture of the Achoma landslide occurred the 18th of June) over the Colca Valley, Peru. The interferograms were generated with the NSBAS processing chain (Doin et al., 2011), at medium spatial resolution. Sentinel-1 data, originally acquired with a ground resolution of 2.3 m in range and 14 m in azimuth, were multilooked (8 and 2 looks in range and azimuth, respectively) to a final pixel size of 18.4 m × 28.2 m. Temporal baselines range from 12 days (the minimum available for the area) to 1 year. The topographic contribution of the signal was removed with the SRTM 30m digital elevation model. The interferograms were not filtered, in order to avoid possible artefacts and loss of deformation signal (Strozzi et al., 2020).

A first inspection of the interferograms was carried out, this revealed a non-linear behaviour of the landslide, characterised by phases of quiescence and activity. The nature of the landcover, largely composed of agricultural land and the intermittent, occasionally strong

displacement gradients cause low coherence and low signal to noise (S/N) ratios in interferograms with temporal baselines of 48 days and longer. The highest signal-to-noise (S/N) ratios are observed for temporal baselines of 12 and 24 days. Thus, for the successive analyses described in the following sections, we selected a series of 113 successive interferograms with the shortest available baselines. Additionally, we included interferograms with baselines of 30, 48, and 72 days to cover periods where shorter baselines are unavailable due to missing images (Figures S1-S8 in supplementary materials). Whilst this approach does not offer the redundancy of image connections required for time series inversion, it allows to cover the observation window with the highest S/N ratio interferograms, whilst limiting the number of gaps over the period.

The boundaries of the Achoma landslide were mapped in geographical coordinates based on geomorphological characteristics observed on Google Earth optical images (Dini et al., 2022). The polygon outline was then projected in the geometry of the radar images. The interferograms were cropped around the landslide polygon, with the crop size (71 by 81 pixels) chosen to provide a margin around the landslide in each direction comparable in size to the landslide itself. This allows for a meaningful comparison between the area inside the landslide and the surroundings as well as for the presence of areas assumed stable (not affected by displacements) and characterised by good temporal interferometric coherence (equal to or higher than 0.4). A 5 x 5 pixels window was used to calculate coherence, γ , as:

$$\gamma = \frac{|\langle S_1 \cdot S_2^* \rangle|}{\sqrt{\langle S_1 \cdot S_1^* \rangle \langle S_2 \cdot S_2^* \rangle}} \quad (1)$$

where $\langle \cdot \rangle$ is the complex conjugation averaged over the chosen window and S_1 and S_2 are the complex values of primary and secondary images composing an interferogram (Dini et al., 2022; Kumar and Venkataraman, 2011).

In the following sections, we illustrate: 1) the removal of the component of the phase signal proportional to perpendicular baselines from the raw interferograms, to identify and mitigate any residual component associated with topographic errors; 2) the analysis of coherence loss

patterns; 3) the analysis of the raw phase signal and its changes over time; and 4) the analysis of the influence of seismicity, rainfall, and river erosion on the landslide's recent history.

3.2. Topographic error correction of raw interferograms

An area assumed stable (i.e., not affected by ground displacements) was chosen outside the landslide boundaries. Various window sizes were tested for this area, and a 5 x 5 pixel window was ultimately chosen—large enough to provide a more meaningful average of phase values than a single pixel, yet small enough to avoid including areas with markedly different ground reflectivity. The choice of the window was based on the average of a proxy of the temporal coherence, as defined by Thollard et al. (2021), ensuring phase stability, this was followed by a visual analysis of the geomorphological features in the proximity of the landslide. The phase of each wrapped interferogram (prior to landslide failure) was referenced to the mean phase of the selected stable reference window, $e^{i\varphi_{k,ref}}$, computed for each interferogram, *k*, by multiplying the interferometric phase of all pixels by the complex conjugate of the average phase within the reference window (Dini et al., 2022). After this referencing step, the influence of the perpendicular baseline on the phase values of individual pixels within each interferogram was analysed. Higher perpendicular baselines cause higher sensitivity to topography (Colesanti and Wasowski, 2006; Meyer and Sandwell, 2012), therefore, if topographic residuals exist after the topographic component removal with the SRTM digital elevation model, a correlation between baselines and interferometric phase would be revealed. Such topographic residual might be associated with low DEM accuracy or changes of ground surface occurred after DEM acquisition and prior to SAR images acquisition. To do this, we computed the average phase over 5 x 5 moving windows, l, over the entire crop, noted $e^{i\varphi_{k,l}}$. To account for the circular nature of phase values (modulo 2π), a parameter search was carried out to determine the best linear fit within the complex domain. For each moving window, predicted values were calculated as:

$$e^{i\widehat{\delta\varphi}_{k,l}} = e^{iX_k\beta_l} \quad (2)$$

where $e^{i\widehat{\delta\varphi}_{k,l}}$ is the predicted phase in each window l of interferogram *k*, X_k is the perpendicular baseline of each interferogram and β_l is the proportionality coefficient

between $e^{i\delta\varphi_{k,l}}$ and the perpendicular baseline for the window l (Dini et al., 2022). During the parameter search, multiple bounds for β were tested before selecting -0.5 and 0.5 rad/m, with a step size of 0.001. The value of β is determined by maximising the coherence ρ_k between the predicted and observed values given by:

$$\rho_k = \left| \frac{\sum_k e^{i\varphi_{k,l}} * e^{i\widehat{\delta\varphi}_{k,l}}{}^*}{N} \right| \quad (3)$$

where *N* is the number of interferograms (Dini et al. 2022). Maps of β, ρ and corrected interferograms were generated. An example of the relationship between phase and perpendicular baseline for all interferograms is shown in figure 2.

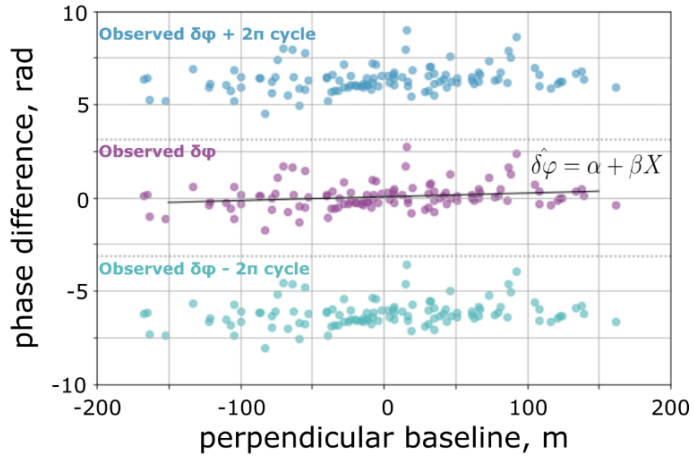

Figure 2. Example of correlation between phase and perpendicular baseline for one moving window. Each purple point represents the complex average phase in the sample window for a given interferogram with respect to the complex average phase in the reference area. As the phase is known in modulo 2π, its +2π and -2π values are also shown in blue and teal respectively. (Modified from Dini et al. 2022, Gretsi Colloque Proceedings).

3.3. Coherence loss analysis

Interferometric coherence and its changes within the landslide and in the surrounding area were analysed both in space and time, in a qualitative and quantitative way respectively. We retained all the selected 113 successive interferograms for this analysis, irrespective of their average coherence. This is because if coherence is to be used as a precursory indicator, its potential should be tested over a range of interferograms, including those in which the phase might be unreliable. Spatial coherence loss is identified within individual interferograms. We focused on patterns of coherence loss over confined areas, as a proxy of localised strain: localised and spatially organised changes of the complex interferometric values are likely

associated with localised displacements, particularly if these correspond to gravitational morphological features (e.g. scarps or extensional structures associated with gravitational slope movements).

In order to detect changes in mean coherence through time and between the landslide and the surrounding gravitationally stable areas, we first calculated for each interferogram the average coherence over the whole crop, along the scarp and within the mapped landslide boundaries. The scarp and crown areas are key locations for precursory detection as motion related to retrogression might be focused here. Boundaries for the scarp were mapped on Google Earth optical images on the basis of geomorphological features and then converted in radar coordinates, as for the landslide boundaries. We analysed the average coherence time series in relation to daily rainfall, downloaded from the online platform of the national service of Meteorology and Hydrology of Peru (Servicio Nacional de Meteorología e Hidrología del Perú) (see section 3.6.2 for further details). We then computed the time series of the ratio between average landslide coherence and average coherence of the surrounding area (Jacquemart and Tiampo, 2021). The ratio is chosen because it highlights changes occurring in the landslide with respect to the surroundings, whilst accounting for periods of coherence loss associated to vegetation changes or ground moisture changes due to rainfall events that would affect the coherence everywhere in a similar way. The changes highlighted by such ratio are therefore most likely associated with ongoing deformation inside the landslide area. In our method, coherence is interpreted relative to a local surrounding area rather than across a large region or the entire SAR frame. As mentioned in section 3.1, we selected the size of the surrounding area so that it is comparable to the landslide footprint, serving as a baseline for normal variability, but not too large to avoid including very different noise sources. Thus, this approach does not require the landslide to stand out across a much larger area; rather, the key signal emerges from local deviations detectable over a few km scale. A temporal mean coherence was computed for each pixel and compared to background terrain using z-scores (see supplementary materials and Figure S9).

3.4. Wrapped phase analysis

As explained in section 1, the presence of interferograms with a high displacement gradient and/or low S/N ratio hinders the ability to perform reliable phase unwrapping without errors during phases of landslide acceleration. We thus adopted the following procedure to analyse

317 the wrapped phase signal in time, whilst avoiding phase unwrapping. Following an approach
318 similar to that presented in López-Quiroz et al. (2009), we selected 5 interferograms
319 characterised by high S/N ratio and by relatively low displacement gradients. In particular, we
320 ensured to select only interferograms in which the observed displacements gradients would
321 not exceed 2π over the landslide area. The visual inspection of all wrapped interferograms
322 revealed that the area affected by displacements has a similar spatial pattern until failure and
323 that the displacement gradient, as observed in interferograms with higher S/N ratio, has the
324 same sign throughout (which is expected in gravitational motion). For the five chosen
325 interferograms we added 2π to all pixels with phase value < -1 rad, thus obtaining a pattern
326 with values comprised between -1 and 5.28 rad. We then averaged these interferograms,
327 obtaining what we will refer as a model deformation pattern (Figure 3A). We cut the area
328 closely around the deformation pattern over 33 by 33 pixels, in order to reduce the
329 contribution of noise in the surrounding area. We then used this model pattern to investigate
330 its correlation with all 113 interferograms in the series, so that:
331

$$e^{i\widehat{\delta\varphi}_{k,p}} = e^{iM_p\alpha_k} \quad (4)$$

332

333 where $e^{i\widehat{\delta\varphi}_{k,p}}$ is the predicted phase value at pixel *p* of interferogram *k*, M_p is the phase value
334 of the model deformation pattern at pixel *p* and α_k is the proportionality coefficient between

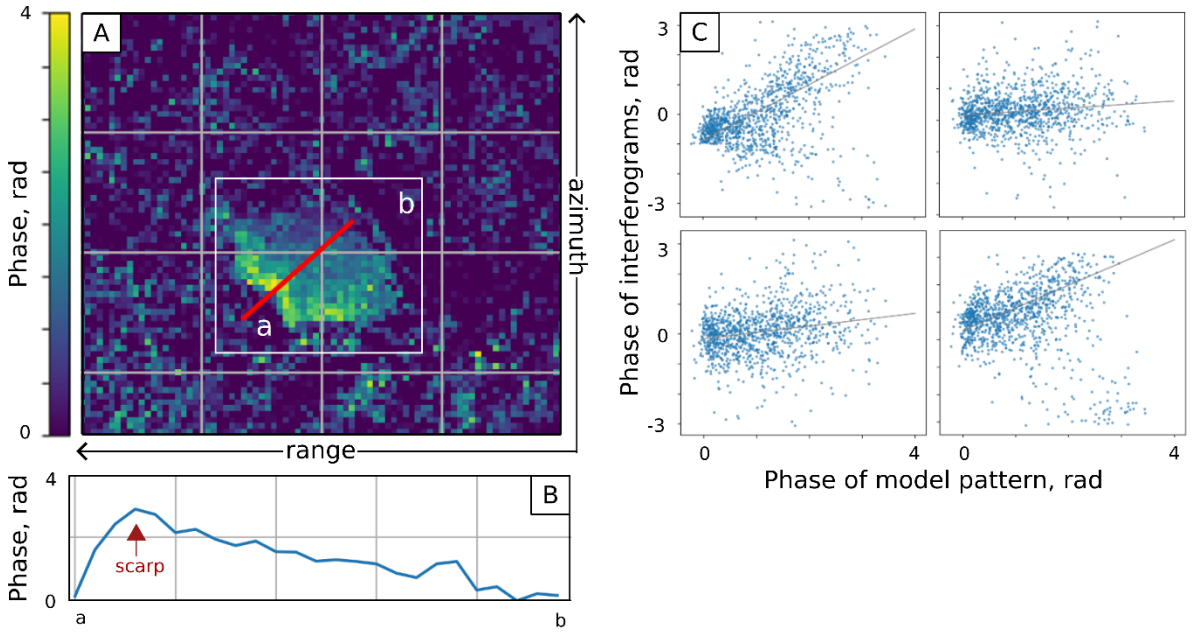

Figure 3. A) Model pattern of deformation in radar coordinates (flipped left-right); B) model pattern phase gradient for the profile a-b; C) examples of four interferograms showing the pixel-by-pixel correlation with the model pattern (from top left, clockwise: 18/08/2018-30/08/2018, 30/08/2018-11/09/2018, 23/09/2018-05/10/2018, 05-10/2018-29/10/2018).

the phase of the model pattern and interferogram *k* (Figure 3B). For the parameter search, -7 and 7 were chosen as bounds for α_k, to account for potentially large displacements that might have affected the landslide in the days/weeks before failure, with a 0.001 step. The value of the proportionality coefficient α_k is then used to represent a dimensionless measure of displacement rates, *DI*, which is a quantity of activity for each interferogram in the series. For example, interferograms characterised by α_k around zero are those with no detectable displacements, whilst α_k around 1 would indicate for interferogram *k* a similar displacement gradient to the model pattern. The value of α_k is obtained by maximising the coherence between the predicted and observed values, the latter a measure of the goodness of fit:

$$\gamma_k = \left| \frac{\sum_k e^{i\varphi_{k,p}} * e^{i\delta\widehat{\varphi}_{k,p}}{}^*}{N_p} \right| \quad (5)$$

where N_p is the number of pixels in interferogram *k*. Successively, the same procedure was applied only to pixels falling within the landslide, masking outside pixels. This was done to generate a ratio between the best coherence calculated over landslide pixels only and the coherence over all pixels, including surrounding area pixels. A low ratio indicates poor fit of

the model within the landslide area in particular, which in turn indicates high likelihood of high displacements gradients leading to spatial aliasing and decorrelation. A threshold of such ratio was set at one standard deviation below the mean value. Unreliable interferograms (grey dots in figure 6) are those with ratio falling below this threshold.

3.5. InSAR-derived downslope displacements

The dimensionless measure of displacement rates, *DI*, obtained with the analysis of raw phase in successive interferograms described in section 2.4 is not an absolute measure of displacements. It represents the degree of activity within the landslide in the time interval covered by each interferogram, as it reflects the correlation between the model pattern and each interferogram. Figure 3C shows a profile across the model that runs along the maximum slope gradient roughly, through the middle of the landslide. The highest values are observed at the scarp, with a maximum value, r_{max}, of 3.45 radians, decreasing to around zero at the toe of the landslide. Therefore, to estimate line of sight (LOS) displacements in mm, we rescaled the dimensionless displacement rates, *DI*, as:

$$DI_{mm} = DI * r_{max} * \frac{\lambda}{2\pi} \quad (6)$$

where λ is the half the wavelength of the satellite, which for Sentinel-1 is 28 mm.

An assumption generally accepted for landslides is that the displacement vector is oriented along a line of maximum slope gradient (Notti et al., 2012). This reflects the overall motion of the landslide, even if, unless the landslide is a pure translational slide, some parts of compound landslides have higher vertical component of the displacements than others. Following the approach presented in Notti et al. (2012), we computed a coefficient that describes the percentage of downslope displacement that is detectable along the line of sight and applied a correction to the displacements. This coefficient is 0.88, for an incidence angle over the area of 40.7 degrees, a heading angle of 347 degrees, and average slope and aspect of 17 degrees and 74 degrees respectively.

We then applied a correction to the displacements obtained with the optical image correlation, *DO*, described in section 2.4, once again assuming that the displacements occur along the maximum slope gradient and taking an average slope angle of 20 degrees, so that:

$$DO_{mm} = \frac{DO}{sin\ (\vartheta)} \quad (7)$$

where ϑ is 70 degrees, the complementary to the average slope angle.

Finally, we identified the onset of activity periods in the InSAR time series, we fitted for each period a linear model. We then computed the slope of the curve for each phase and compared the values at different ones.

3.6. External forcing

In order to detect external events that may have played a role in the onset of activity at specific times, we took into consideration seismicity, rainfall and maximum river width as a proxy for erosion. The pore pressure increase associated with rainfall (Agliardi et al., 2020; Carey et al., 2019) and seismic shaking (Lacroix et al., 2022b) is an important factor that perturbs the internal stress state of the rupture surface of large landslides, inducing slip onset (Agliardi et al., 2020). River erosion also plays a role in modulating landslide activity in the region (Lacroix et al., 2015) and increased fluvial erosion might increase landslide activity by removing material at the toe (McColl, 2022), undercutting the slope (Ballantyne, 1986; Fourniadis et al., 2007; Yang et al., 2021) and potentially exposing the sliding surface.

3.6.1. Earthquakes

We computed a comprehensive list of earthquakes with magnitude 3 and above, occurred within a radius of 150 km of the Achoma landslide, between 2015 and July 2020 from the online platform of the Geophysical Institute of Peru's (Instituto Geofísico del Peru). The list comprises of 361 events. For each event, we calculated the expected peak ground acceleration (PGA, m/s^2) as indicator of seismic ground motion at the Achoma landslide site by applying the ground motion prediction method ofAkkar and Bommer (2010). This method was shown by previous studies to perform well for a landslide site located approximately 10 km west of the Achoma landslide (Bontemps et al., 2020; Lacroix et al., 2015). PGAs of 0.1 m/s^2 and above are obtained for earthquakes occurred at less than 50 km from the landslide, with magnitudes comprised between 3.8 and 5.6, except for one event, occurred at 84 km, but with magnitude 6.2.

3.6.2. Rainfall

Hourly rainfall data starting from 2015 recorded at the station of Chivay, approximately 9 km northeast of the landslide site, at a similar elevation, were downloaded from the online platform of the National Service of Meteorology and Hydrology of Peru (Servicio Nacional de Meteorología e Hidrología del Perú). This was then converted into daily rainfall totals. Cumulative rainfall for each dry-rainy season sequence (August to August of following year) has been plotted for every year, to compare activity rates with rainfall. 2015 and 2016 were characterised by drier conditions than following years. To identify more intense daily rainfall events, characterised by higher 24 hours cumulative rainfall, we computed the histogram of daily rainfall, which presents a skewed right distribution. We selected a threshold of 25 mm/day as the intense rainfall event, as frequencies of higher daily totals do not exceed 1 in the whole observation period.

3.6.3. River erosion

As a proxy for river erosion at the landslide's toe, we analysed the changes in river width over time. To accomplish this, we utilised 219 Planet Lab PlanetScope images with 3m ground resolution. We selected three sections along the river: one in the middle of the landslide and one at each boundary. For each image, we measured the river's width at each of the three locations. The river's width broadly follows a seasonal pattern corresponding to the seasonal rainfall over the area, implying that the river's erosive power follows a similar temporal pattern to the rainfall. However, our objective was to identify unseasonably large river events that might be triggered by localised events upstream in the catchment, which are not directly recorded at the nearby meteorological station. To identify such unseasonable events, we computed a rolling mean of the river width and looked for peaks exceeding one standard deviation from the mean. In addition to this, we mapped the riverbanks at maximum width for each year, to determine any position changes through time that might be indicative of persistent, significant erosion.

4. Results

4.1. Spatial coherence features as long-term precursors

Interferometric coherence maps generated for all selected successive interferograms (see section 2) exhibit distinct, consistent features over the observation period (figure 4). Notably,

low coherence lineaments appear intermittently up to 5 years before the landslide failure. These features manifest as narrow, rope-like structures located primarily along the scarp and southeastern flank of the landslide, consistent with post-failure observations. Interestingly, these features persist even in interferograms characterised by generally low coherence, where phase unwrapping would typically be unreliable. They are identifiable in 25 interferograms spanning from the earliest available (covering the period 30th April 2015 to 11th July 2015) up until 16th March 2020, approximately three months prior to the failure. Pixels intersecting the scarp exhibit significantly lower coherence than the surrounding area (Welch's t-test, $p < 0.001$; see supplementary materials and Figure S9). Starting from 9th April 2020 the entire area affected by the landslide shows a more widespread loss of coherence, indicative of a regime shift.

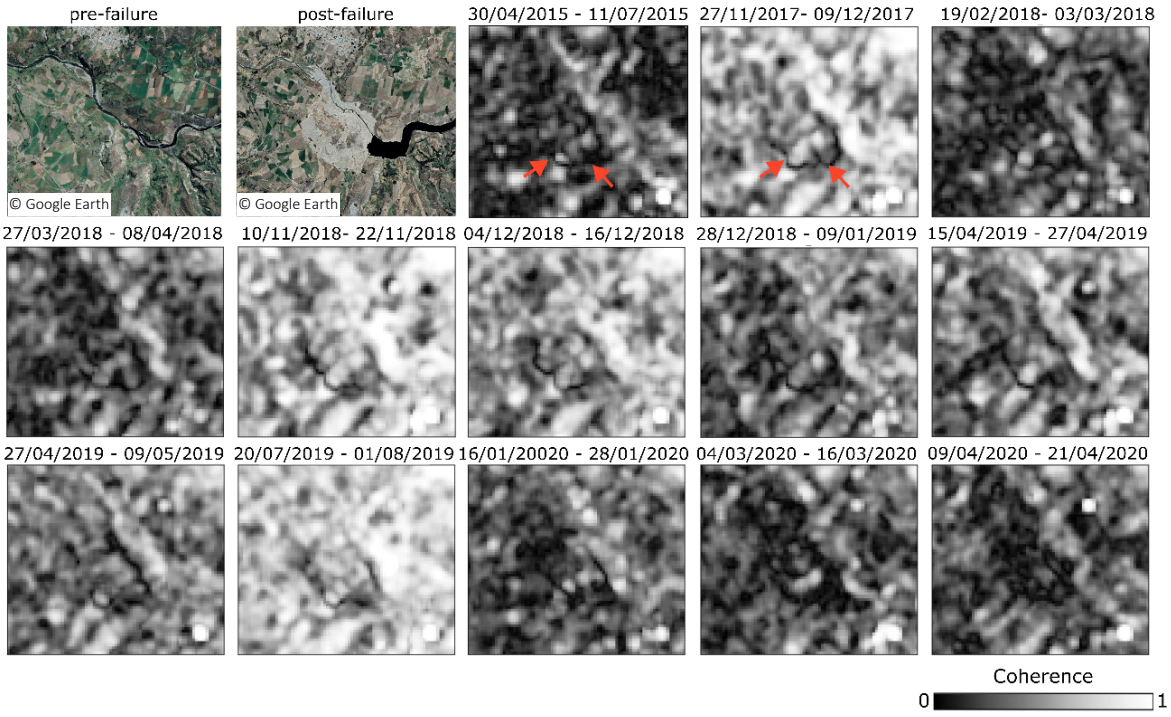

Figure 4. Pre- and post-failure ©Google Earth pre-failure (29/04/2019) and post-failure images (1/11/2020), with a series of interferometric coherence examples showing the development of headscarp and southern boundary, with the change in regime from March 2020.

4.2. Time series of coherence ratio

Figure 5A illustrates the average coherence in the landslide area and in the surrounding area. Albeit with some small differences, the coherence drops everywhere following similar temporal patterns during the rainy seasons. The coherence ratio between the landslide and

the surrounding area (figure 5B) remains around 1, with a mean of 0.98, from 30th April 2015 to 28th March 2020, encompassing multiple wet seasons. Subsequently, starting from this date until the failure on 18th June 2020, the ratio progressively declines below 0.8, reaching its lowest value of 0.19 at the time of failure. The significant drop in the coherence ratio three months prior to failure indicates that the landslide area was losing coherence faster than its immediate and directly comparable surroundings.

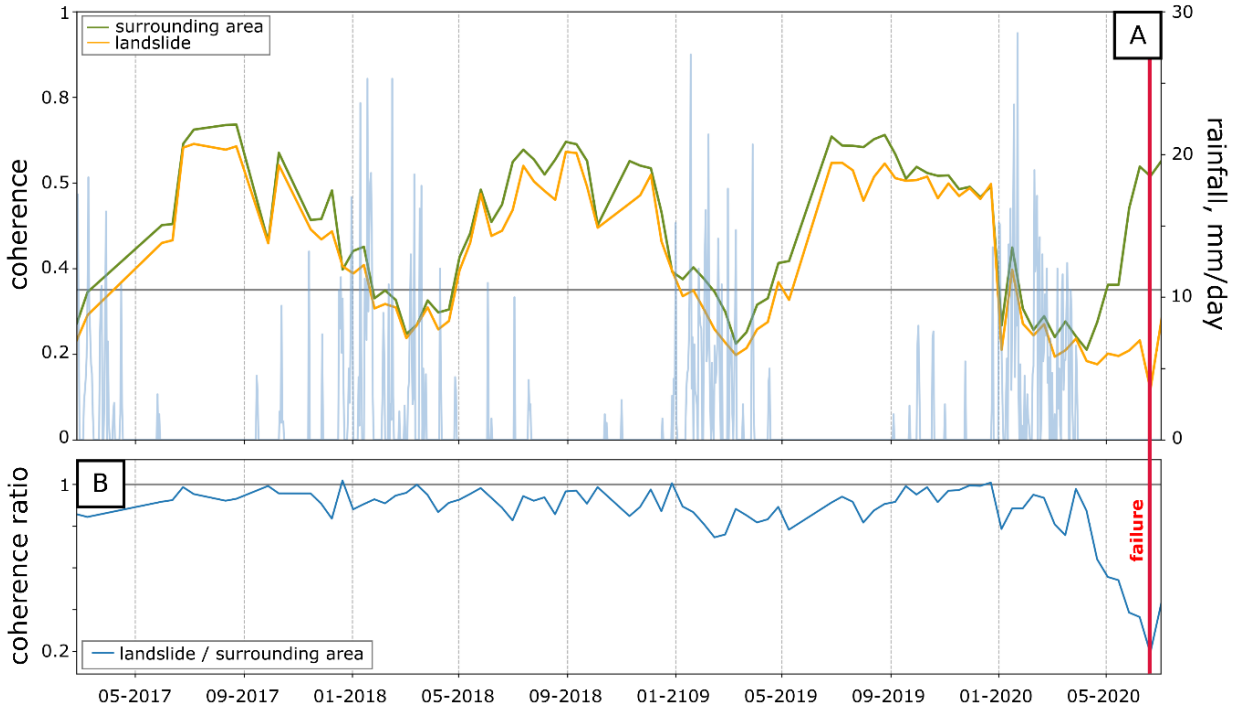

Figure 5. A) Interferometric coherence for different parts of the landslide, superposed on daily rainfall. B) Coherence ratio. Failure is indicated by the vertical red line.

4.3. Acceleration phases as seen by InSAR

The dimensionless activity index time series, derived using the method outlined in section 2.5, is shown in figure 6. The time series reveals periods of relative stability interspersed with phases of acceleration. Transient creep events are characterised by displacements occurring within individual or, in one case, over two consecutive interferograms amid periods of minimal long-term displacements. Four transient creep events between April 2015 and August 2016 exhibit dimensionless displacement rates exceeding 1, occurring amidst a backdrop of rates generally around 0 and less than 0.25 (Figure 6; Table 1). The displacements

observed in these interferograms match or exceed the mean deformation pattern shown in figure 3A. In contrast, we observe long acceleration phases, periods during which displacement rates increase significantly over three successive interferograms or more. These become apparent from November 2017 onwards.

Four distinct acceleration phases are observed:

- Phase 1: 27th November 2017, to 8th April 2018
- Phase 2: 19th June 2018, to 9th May 2019
- Phase 3: 8th July 2019, to 20th July 2019
- Phase 4: 4th January 2020, to 4th March 2020 (culminating in failure 3 months later)

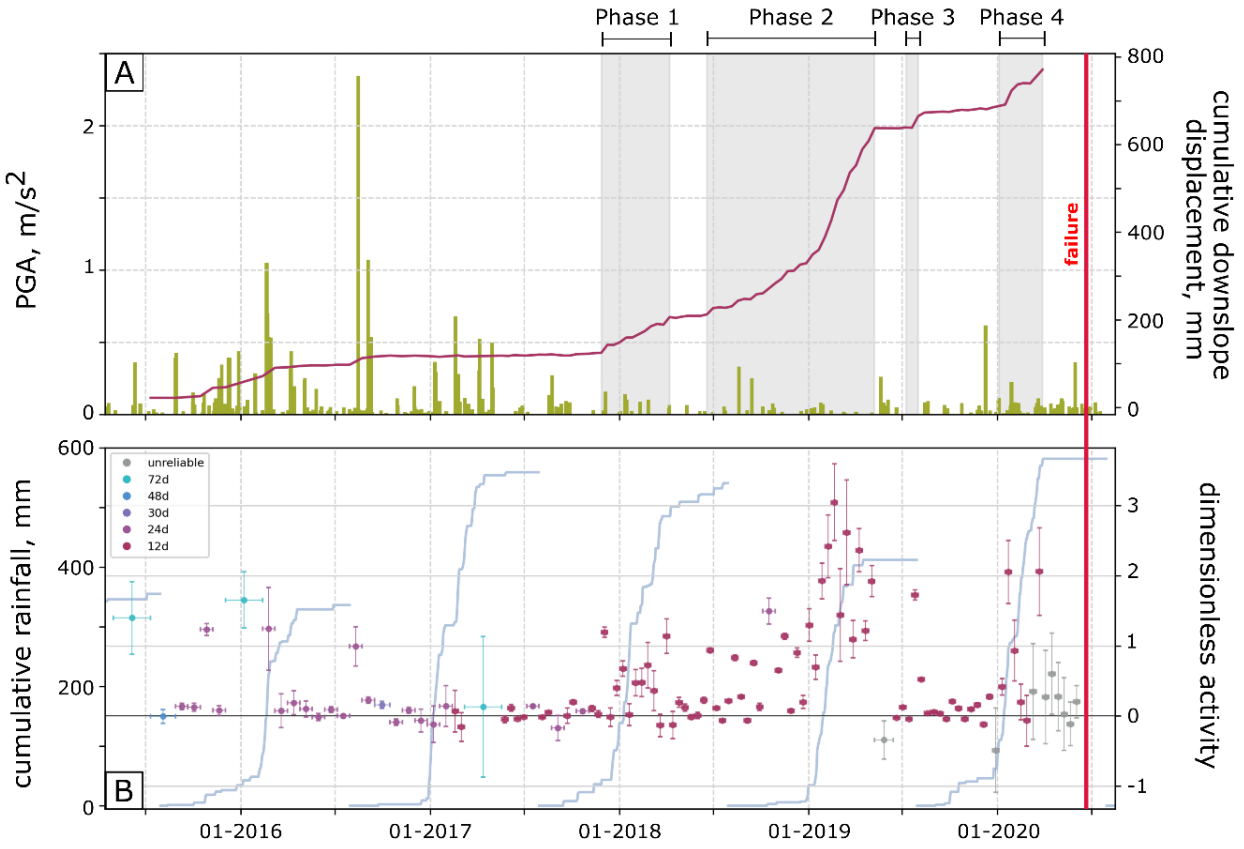

Figure 6. A) purple curve, estimated downslope cumulative displacement in mm after correction; green bars, PGA. B) dimensionless activity index, every dot represents an interferogram, different colours and horizontal bars represent interferogram duration, vertical bars $1/\gamma_k$ normalised by its max value (eq 5); blue curves, cumulative rainfall over the rainy season.

The accelerations are detected using the dimensionless index (see section 2.4), but we present below the estimated rates (see section 2.5), for ease of description.

The first acceleration begins with an initial significant displacement (~18 mm in 12 days), followed by a period of linear displacements over 132 days at an almost steady rate of approximately 279 mm/year.

The second phase follows a 10-week quiescence period and exhibits escalating trends: 234 mm/year between 19th June 2018, and 5th October 2018; 425 mm/year between 5th October 2018, and 9th January 2019; and 1080 mm/year between 9th January 2019, and 9th May 2019. A short acceleration in July 2019 transitions quickly into a brief period stability followed by a phase of low, steady-rate creep from 1st August 2019 to 23rd December 2019, characterised by a gentle trend of 38 mm/year. This is succeeded by the last acceleration phase, reaching approximately 567 mm/year from 4th January 2020 to 4th March2020, the last reliable interferogram captured, then culminating in failure.

5. Discussion

5.1. Spatial patterns of low coherence

The coherence maps derived from successive interferograms reveal slope instability by delineating gravitational morphological structures dating back five years before failure. In the earliest available interferogram (30th April 2015 – 11th November 2015), a distinct low coherence boundary is evident despite the low average coherence, closely mirroring the later spatial development of the landslide. The low-coherence markers likely indicate areas of strain resulting from landslide displacement, marking the boundary between stable and unstable ground. These markers are interpreted as early signs of destabilisation, suggesting strain concentration along the failure surface is beginning to occur, albeit with very small displacements. We observed similar features in other landslides in the Colca Valley, indicating that these signals are not isolated occurrences and highlighting their importance and reliability for early detection at large scales. Some of these landslides have exhibited long-term creep without progressing to catastrophic failure. In these cases, low-coherence markers appear to indicate retrogressive behaviour with the formation of secondary scarps over the years and delimiting different activity sectors.

5.2. Factors influencing coherence loss

Low interferometric coherence, reflecting high phase variability between adjacent pixels, can be caused by factors like dense vegetation, crops, surface debris, snow, or spatial heterogeneity of ground deformation. In the case of the Achoma landslide, the low coherence markers observed are unlikely to be caused by localised land cover changes. Instead, they likely reflect slight differential displacements associated with the development of surface discontinuities. These features have been observed up to three months before failure, similar to the final acceleration stage detected with optical images by Lacroix et al. (2023). Jacquemart et al. (2021) discuss various factors contributing to interferometric coherence loss in landslides, including soil moisture changes, erosion, vegetation dynamics, and active slope deformation. While distinguishing between these causes is challenging, their combined presence suggests increased landslide activity.

The observed transition in coherence patterns, from localised anomalies along gravitational structures to widespread loss across the entire landslide area in March 2020, points to significant shift in landslide dynamics. This likely marks the transition from small displacements (with the landslide behaving as a cohesive body) to higher displacement gradients and internal deformation. Identifying such transitions in coherence could provide valuable lead time for early warnings, offering a proactive approach to landslide monitoring in previously unmonitored areas.

5.3. Coherence ratio analysis

In addition to the spatial patterns of low coherence, we analysed the ratio between the mean coherence over the landslide area and that in the surrounding area, using a methodology similar to that adopted by Jacquemart and Tiampo (2021). This ratio helps account for temporal coherence variability that affects both the landslide and its surroundings similarly. For example, seasonal moisture changes can impact coherence, but the ratio remains close to 1 unless changes occur specifically within the landslide area.

A noticeable drop in the coherence ratio occurred approximately three months before the failure event, beginning around 4th March 2020. By setting a retrospective threshold (one standard deviation below the mean coherence ratio), we identified that this threshold was surpassed between 9th and 21st April 2020, indicating predictive value about two months before the Achoma failure. Jacquemart and Tiampo (2021) noted a similar coherence ratio decline approximately five months before the Mudcreek landslide, attributing it partly to

549 vegetation degradation. In contrast, our analysis of the Achoma landslide shows a sharp
550 increase in the coherence ratio post-failure, reaching values as high as 1.98 during the 2021
551 rainy season. This increase suggests that vegetation degradation following the failure may
552 expose rock and soil, enhancing phase stability in the absence of displacements. Thus, the
553 observed drop in coherence leading up to failure is likely associated with high displacement
554 gradients leading to increased internal deformation of the landslide mass and phase aliasing.
555 This observation is consistent with the three-month final acceleration stage identified
556 through independent measurements by Lacroix et al. (2023). Further investigation into other
557 case studies is needed to establish universal indicators and thresholds for landslides at critical
558 stages.
559
560 5.4. Dimensionless activity index
561 The InSAR data processed in this work indicates that the Achoma landslide underwent a long
562 evolution. Our observations show that progressive damage and fault maturation over a
563 period of at least five years, likely longer, ultimately led to landslide failure, in agreement with
564 the findings of Lacroix et al. (2023). To simplify, we separately discuss two broad periods,
565 based on different styles of activity observed.
566
567 *April 2015 to December 2017*
568 The key observation is that between April 2015 and December 2017 the long-term activity
569 index for this period reveals short-lived transient creep events in response to perturbations,
570 interspersed with prolonged period of little to no activity (Figure 6; Table 1). This suggests the
571 presence at this stage of a maturing surface of rupture, allowing for some hydro-mechanical
572 fluid-solid coupling (Agliardi et al., 2020), but not yet a self-sustaining process of progressive
573 failure. Displacements during this period may span up to 72 days due to sampling intervals.
574 Between December 2015 and March 2016, a combination of moderate seismicity and rainfall
575 led to possible prolonged displacements over two consecutive interferograms for up to 96
576 days. However, the temporal resolution of the data does not allow us to determine whether
577 movement was continuous or intermittent within these intervals.
578 While the August 2016 earthquake, with the highest PGA of 2.34 m/s^2 recorded during the
579 study period, did result in some movement, it was lower than the movements observed
580 between April 2015 and March 2016. Moreover, although the rainy season of 2016/2017

recorded comparable precipitation totals to subsequent seasons, no prolonged period of acceleration was observed until the end of 2017. This suggests that a combination of seismicity and rainfall may be more critical for driving significant acceleration than either factor alone. Unlike the Maca landslide, which exhibited prolonged post-seismic accelerations following the 20 February and 15 August 2016 earthquakes, lasting 5 months and several weeks, respectively (Bontemps et al., 2020), the Achoma landslide's response was transient and not sustained, as no subsequent interferograms indicated continued movement. Post-seismic motion has been associated to pore-water pressure increases due to sediment contraction (Lacroix et al., 2022b). The absence of post-seismic motion at the Achoma landslide may reflect that the rupture surface was not sufficiently mature, and lacked the necessary pathways for water to migrate from contracted sediments to the rupture zone. Without this migration, the pore pressure at the rupture surface could not build up to a level that would sustain post-seismic motion.

Interferogram dates (and duration in days)	Max PGA m/s^2	Number seismic events	Dimensionless displacement (estimate mm)	Estimate displacement rate mm/yr	Cumulative rainfall mm
30/04/2015 – 11/07/2015 (72)	0.36	6	1.4 (~26)	~132	9.1
15/10/2015 – 08/11/2015 (24)	0.15	4	1.2 (~23)	**~350**	13.1
02/12/2015 – 12/02/2016 (72)	0.44	**26**	1.7 (~31)	~157	56.4
12/02/2016 – 07/03/2016 (24)	**1.05**	9	1.2 (~23)	**~350**	**160.1**
29/07/2016 – 22/08/2016 (24)	**2.34**	7	1 (~18)	**~274**	0

Table 1. Interferograms showing possible transient creep behaviour associated with nearby earthquakes.

December 2017 to June 2020

A shift in behaviour can be identified from December 2017: from this point, longer periods of activity begin to occur. The landslide reacts quickly to the onset of the wet season in December 2017, despite lower seismicity than in the previous period, suggesting that the rupture surface has fully developed and become more sensitive to perturbations. This likely reflects the formation of a fine-grained gouge along the basal shear plane (Agliardi et al., 2020), reducing permeability and altering pore pressure dynamics. These internal changes led to cycles of acceleration, deceleration, and steady-state stages (Zhou et al., 2018) (Figure 6A), driven by transient perturbations like seismic events or rainfall and modulated by mechanisms like pore pressure dissipation (Lacroix et al., 2020) or strain-strengthening

behaviour (Agliardi et al., 2020)ultimately resulting in sustained slip rates even during dry periods. This pattern is particularly evident during the dry season of 2018, when the Achoma landslide exhibited sustained displacement rates despite the absence of significant external triggers. This observation highlights the role of ongoing internal processes, such as continued damage accumulation along the basal shear plane, in maintaining instability and movement over time.

As Lacroix et al. (2023) note, the final stage of acceleration began in the wet season. While optical images from Lacroix et al. (2023) pinpoint the beginning of the final acceleration in March 2020, InSAR-based observations in this study suggest that the landslide began accelerating as early as January 2020, following a period of steady slip rates during 2019. Although rainfall was undoubtedly a key factor, similar rainfall totals in 2017 and 2018 did not lead to failure, suggesting that other factors, such as accumulated damage or changes in the basal shear zone, were more critical in 2020. Increased seismic activity in the final stages, marked by a higher frequency of smaller earthquakes, likely contributed to the landslide's acceleration, demonstrating a combination of driving factors.

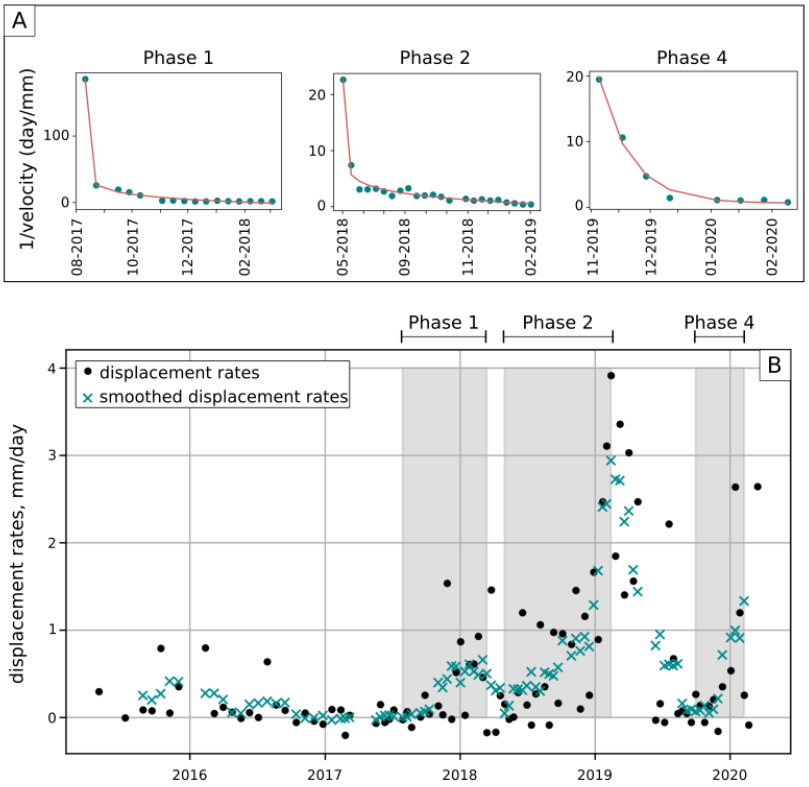

Figure 7. A) 1/velocity plots for phase 1, phase 2, and phase 4. B) Displacement rates for raw (black dots) and smoothed data (blue x, smoothed using a 5-window running mean). Shaded areas show accelerations of phase 1, phase 2 and phase 4.

Figure 7 compares acceleration phases 1, 2, and 4 using inverse velocity (day/mm) plots, derived from the estimated displacements. Although the measure is not an absolute displacement, its evolution reflects distinct kinematic behaviours. Phase 1 begins at a high inverse velocity (>100 day/mm), indicating very slow initial movement and a large relative change during acceleration. Phases 2 and 4 start from lower 1/v values, suggesting a more active baseline state by the time acceleration began. Phases 1 and 2 show an abrupt initial drop followed by flattening at values above zero, consistent with asymptotic decay and indicating the attainment of temporary steady states following transient accelerations (Carlà et al., 2017). In contrast, phase 4 declines more gradually but approaches near-zero inverse velocity within ~3 months, signalling sustained acceleration towards failure rather than stabilisation. This pattern suggests the slope did not fully recover stability between acceleration episodes, supporting the interpretation of progressive internal degradation and gradual accumulation of strain.

While external forcing factors, such as rainfall and seismic activity, modulated the timing and magnitude of these accelerations, they cannot alone explain the observed behaviour. For instance, comparable rainfall totals in 2019–2020 did not trigger failure, and acceleration continued through the 2018 dry season. The 1/v plots highlight the internal process of material degradation, including microcrack formation and coalescence, leading to the development of a shear surface by March 2020. By observing these behaviours, we demonstrate how dimensionless parameters from the wrapped phase can capture meaningful kinematic evolution, offering valuable insight into early destabilisation mechanisms.

Finally, it is worth noting that phase 4 is truncated roughly 3 months prior to failure due to increasing noise in the dimensionless measure, preventing observation of the full 1/v trend as the landslide approaches collapse. These inverse velocity plots are therefore not intended to predict failure timing but to illustrate the changing kinematic behaviour across acceleration phases.

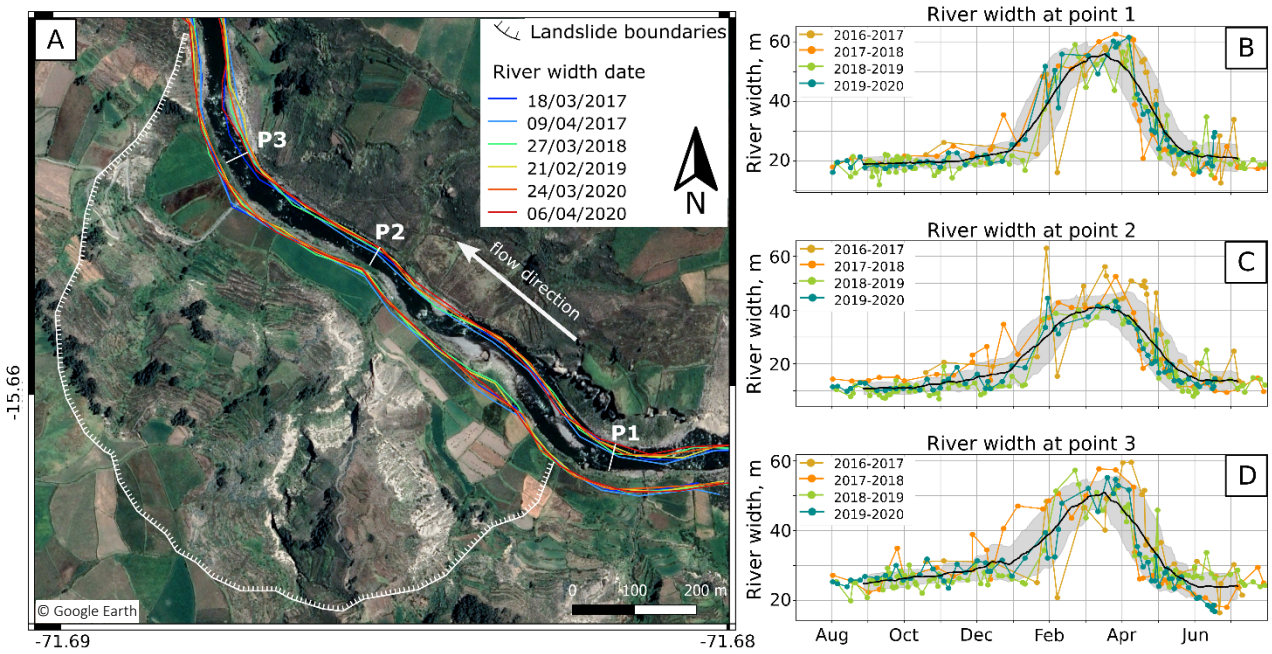

Figure 8. A) Mapping of riverbanks position at maximum width. If date of maximum width differs between P1, P2, P3, multiple dates per wet season are taken (e.g. 2017, 2020). Mapping and annotations are superposed to a ©Google Earth pre-failure (20/04/2019) satellite image. B-D) River widths for P1, P2, P3 respectively. Data is plotted from dry season to dry season the following year. The black curve represents the 40-day running mean, and the grey shading represents one standard deviation above and below the mean.

Figure 8A shows the position of the riverbanks during maximum river width periods for each wet season (2016–2020). Despite potential image resolution limitations, our observations reveal no clear trend of significant erosion toward the left bank or landslide toe. Instead, riverbank positions vary over time, indicating movement in both directions, into and away from the landslide toe. The right bank shows a slight tendency to move away, possibly due to the landslide toe pushing the riverbed, which may increase erosion on that side. River width measurements in Figure 8B-D, used as a proxy for erosional power, do not indicate significant erosion events during the 2020 dry season. These findings suggest that the landslide was not triggered by high river erosion, but rather by a long-term process of progressive failure.

5.5. Complementarity

Our observations highlight variations in the Achoma landslide's response to triggers, depending on its stage of basal shear plane maturation, suggesting that different processes were involved. We retrospectively identify the beginning of a final acceleration already in January 2020 (as shown by wrapped phase dimensionless activity marker), transitioning into

a critical and irreversible instability in March 2020 (as shown by coherence both in space and time), indicating that proactive monitoring could have commenced at least at this critical stage. This finding echoes Jacquemart and Tiampo's (2021) observation of a coherence ratio drop five months before the failure of the Mudcreek landslide, emphasising its potential as early indicator. They also noted that an approach based on time series generation underestimated displacements. In contrast, (Handwerger et al., 2019)used a preprocessing step for signal removal before unwrapping in their analysis of the same landslide. Our method, leveraging wrapped phase analysis, offers a more streamlined alternative, providing valuable insights into landslide evolution without complex preprocessing. Unlike traditional InSAR approaches requiring signal removal and reintroduction, our method is less time-consuming and demonstrates the effectiveness of analysing the wrapped phase. In addition to this, integrating InSAR-based signals with optical time series enhances the understanding of landslide dynamics across different phases. The metrics we propose identify areas of incipient strain and early acceleration phases, while optical time series capture the final acceleration phase characterised by larger displacements (Figure S10 in supplementary materials).

The indicators proposed here rely on the identification of critical features, such as gravitational structures in the coherence signal or the moving mass in the wrapped phase. In practice, wrapped phase patterns could also be used to delineate the boundaries of potentially unstable zones, which can serve as the basis for coherence ratio analyses to assess localised changes relative to their surroundings. While the observed coherence and phase signals are promising indicators, determining whether they can be reliably detected without prior knowledge of landslide locations will require large-scale analysis across diverse terrains, likely combining InSAR with topographic, geomorphic, and signal-specific characteristics. Evaluating the generalisability of this methodology across different landslide types and settings is a key goal for future work. Furthermore, automated detection of these features using machine learning techniques could significantly enhance landslide monitoring. Approaches such as that proposed by Chen et al. (2022) demonstrate the feasibility of applying deep semantic segmentation to recognise active landslides from InSAR. Implementing similar AI-driven frameworks on the precursors identified here could automate the detection of early instability signs, reducing reliance on manual interpretation and providing an efficient first filter for identifying destabilising slopes across large areas. Finally,

the approach proposed here could be highly complementary to recent optical monitoring methods aimed at detecting slow-moving landslides. For instance, Van Wyk de Vries et al. (2024)demonstrated that automated Sentinel-2 feature tracking can identify surface deformation for landslides attaining larger velocities than InSAR can detect, providing valuable information on spatial displacement patterns where optical contrast and cloud-free conditions permit. In contrast, InSAR-based coherence and wrapped-phase indicators may be more sensitive to subtler or intermittent deformation and are less dependent on illumination or atmospheric conditions. Furthermore, it is worth noting that the rates of ground deformation detectable with InSAR and optical vary significantly, allowing for the detection of different phases, as shown in this work. Integrating both datasets could therefore improve the detection of a broader spectrum of slope processes, from slow or incipient deformation to more rapid movement phases and enhance confidence in precursor identification by combining independent observational evidence.

6. Conclusions

Using Sentinel-1 interferograms with non-overlapping short temporal baselines, we identified precursors to the Achoma landslide. Our approach bypasses traditional unwrapping and time series generation, revealing significant spatial coherence loss that indicates gravitational features linked to strain localisation along the rupture surface, visible five years prior to failure. Intermittent coherence loss from approximately five years to five months before failure suggests the progressive development of a hydro-mechanically coupled rupture surface with increasing damage concentration. This is further supported by the acceleration, steady-state, and deceleration phases observed in the wrapped phase analysis. Our findings demonstrate the potential of satellite-based InSAR to detect destabilisation precursors before large displacements occur, particularly when continuous displacement time series are hindered by land cover or landslide behaviour. By integrating key parameters and their spatiotemporal changes, this methodology could enhance the identification of precursors over larger areas than traditional time series methods alone, making satellite-based monitoring even more valuable for landslide prediction. However, we acknowledge that not all landslides exhibit measurable precursory motion. For example, rapid, shallow failures in unconsolidated materials

may occur with little to no detectable warning. The approach presented here is therefore likely applicable to large, complex landslides with long histories of slow deformation for which strain accumulation can be capture, and further research across a broader range of case studies is needed to validate coherence loss patterns as reliable precursors for landslides with minimal ground displacement. In this context, a key next step will be to extend this work to regional studies to capture landslides in diverse geological and climatic settings, with different sizes, mechanisms and material composition, to determine more broadly under which conditions similar precursory patterns would emerge and how can they be objectively characterised.

Our findings are nevertheless significant for two practical reasons. First, the Achoma landslide went unnoticed until shortly before failure, a common issue in landslide science where monitoring typically begins after events occur rather than during early precursor stages. Identifying reliable precursors in satellite data could improve landslide prediction on both local and broader scales. While our analysis demonstrates the potential for satellite-based detection of precursory signals, effective early warning ultimately depends on coupling such remote observations with local monitoring and community awareness. Second, the challenge of monitoring landslides only after failure limits the capture of earlier instability phases. Proactively targeting destabilising slopes for instrumentation is critical for effective hazard assessment, failure prediction, and understanding underlying processes. A complementary approach that combines the strengths of InSAR and optical time series, while leveraging AI for automated feature detection, holds remarkable potential for advancing real-time landslide monitoring. Such innovations are key to enhancing community resilience by enabling early detection and supporting timely response and preparedness in landslide-prone regions.

Statements and Declarations

Authors Contribution

BD conceived the idea submitted for CNES fellowship application, PL and MPD helped shape the research. PL brought previous knowledge for the case study and contributed to

conceptual ideas. BD and MPD designed the method for InSAR-based precursors. BD generated the codes and carried out the analysis. BD, PL and MPD contributed to interpretation. BD wrote the manuscript, PL and MPD provided critical feedback.

Funding

This study was carried out as part of a 2-year CNES funded fellowship to Benedetta Dini. The fellowship was undertaken at ISTerre (Universite Grenoble-Alpes)

Competing Interest

The authors declare no competing interests.

Data availability

Sentinel-1 SAR data is freely available from the Copernicus Data Browser at https://browser.dataspace.copernicus.eu/. Rainfall data are provided by SENAMHI and can be downloaded from https://www.gob.pe/senamhi. Seismic data provided by the Instituto Geofísico del Perú are available at https:www.gob.pe/igp. PlanetScope images are available from Planet Lab at https://www.planet.com/. The processed wrapped interferograms and coherence images used in this study have been deposited in Zenodo: Dini, B. (2025): Wrapped interferograms and coherence Achoma landslide, https://zenodo.org/records/17602759. Auxiliary data and python scripts required to reproduce the analysis presented in this paper are also archived in Zenodo: Dini, B. (2025), Auxiliary data and analysis scripts for the Achoma landslide study, Zenodo, https://zenodo.org/records/17753976. All datasets necessary to reproduce the figures and analysis are therefore publicly available.

References

Agliardi, F., Scuderi, M. M., Fusi, N., and Collettini, C.: Slow-to-fast transition of giant creeping rockslides modulated by undrained loading in basal shear zones, Nat Commun, 11, 1–11, https://doi.org/10.1038/s41467-020-15093-3, 2020.

Akkar, S. and Bommer, J. J.: Empirical equations for the prediction of PGA, PGV, and spectral accelerations in Europe, the Mediterranean region, and the Middle East, Seismological Research Letters, 81, 195–206, https://doi.org/10.1785/gssrl.81.2.195, 2010.

Badoux, A., Graf, C., Rhyner, J., Kuntner, R., and McArdell, B. W.: A debris-flow alarm system for the Alpine Illgraben catchment: design and performance, Natural Hazards, 49, 517–539, 2009.

Ballantyne, C. K.: Landslides and slope failures in Scotland: a review, Scott Geogr Mag, 102, 134–150, https://doi.org/10.1080/00369228618736667, 1986.

Berardino, P., Fornaro, G., Lanari, R., and Sansosti, E.: A new algorithm for surface deformation monitoring based on small baseline differential SAR interferograms, IEEE Transactions on Geoscience and Remote Sensing, 40, 2375–2383, 2002.

Bontemps, N., Lacroix, P., Larose, E., Jara, J., and Taipe, E.: Rain and small earthquakes maintain a slow-moving landslide in a persistent critical state, Nat Commun, 11, 1–10, https://doi.org/10.1038/s41467-020-14445-3, 2020.

Carey, J. M., Massey, C. I., Lyndsell, B., and Petley, D. N.: Displacement mechanisms of slow-moving landslides in response to changes in porewater pressure and dynamic stress, Earth Surface Dynamics, 7, 707–722, 2019.

Carlà, T., Intrieri, E., Di Traglia, F., Nolesini, T., Gigli, G., and Casagli, N.: Guidelines on the use of inverse velocity method as a tool for setting alarm thresholds and forecasting landslides and structure collapses, Landslides, 14, 517–534, 2017.

Carlà, T., Intrieri, E., Raspini, F., Bardi, F., Farina, P., Ferretti, A., Colombo, D., Novali, F., and Casagli, N.: Author Correction: Perspectives on the prediction of catastrophic slope failures from satellite InSAR (Scientific Reports, (2019), 9, 1, (14137), 10.1038/s41598-019-50792-y), Sci Rep, 9, 1–9, https://doi.org/10.1038/s41598-019-55024-x, 2019.

Cheaib, A., Lacroix, P., Zerathe, S., Jongmans, D., Ajorlou, N., Doin, M.-P., Hollingsworth, J., and Abdallah, C.: Landslides induced by the 2017 Mw7. 3 Sarpol Zahab earthquake (Iran), Landslides, 19, 603–619, 2022.

Chen, X., Yao, X., Zhou, Z., Liu, Y., Yao, C., and Ren, K.: DRs-UNet: A Deep Semantic Segmentation Network for the Recognition of Active Landslides from InSAR Imagery in the Three Rivers Region of the Qinghai–Tibet Plateau, Remote Sens (Basel), 14, 1848, 2022.

Colesanti, C. and Wasowski, J.: Investigating landslides with space-borne Synthetic Aperture Radar (SAR) interferometry, Eng Geol, 88, 173–199, 2006.

Cook, K. L., Rekapalli, R., Dietze, M., Pilz, M., Cesca, S., Rao, N. P., Srinagesh, D., Paul, H., Metz, M., and Mandal, P.: Detection and potential early warning of catastrophic flow events with regional seismic networks, Science, 374, 87–92, 2021.

Costantini, M., Minati, F., Trillo, F., Ferretti, A., Novali, F., Passera, E., Dehls, J., Larsen, Y., Marinkovic, P., Eineder, M., Brcic, R., Siegmund, R., Kotzerke, P., Probeck, M., Kenyeres, A., Proietti, S., Solari, L., and Andersen, H. S.: European Ground Motion Service (EGMS), in: 2021 IEEE International Geoscience and Remote Sensing Symposium IGARSS, 3293–3296, https://doi.org/10.1109/IGARSS47720.2021.9553562, 2021.

Dini, B., Manconi, A., and Loew, S.: Investigation of slope instabilities in NW Bhutan as derived from systematic DInSAR analyses, Eng Geol, 259, https://doi.org/10.1016/j.enggeo.2019.04.008, 2019.

Dini, B., Manconi, A., Loew, S., and Chophel, J.: The Punatsangchhu-I dam landslide illuminated by InSAR multitemporal analyses, Sci Rep, 10, 1–10, 2020.

Dini, B., Doin, M.-P., Lacroix, P., and Gay, M.: Satellite-based InSAR: application and signal extraction for the detection of landslide precursors, in: 28° Colloque sur le traitement du signal et des images (GRETSI), Nancy, France, 6–9 Sep 2022, pp. 1233–1236, 2022

Doin, M.-P., Guillaso, S., Jolivet, R., Lasserre, C., Lodge, F., Ducret, G., and Grandin, R.: Presentation of the small baseline NSBAS processing chain on a case example: The Etna deformation monitoring from 2003 to 2010 using Envisat data, in: Proceedings of the Fringe symposium, 3434–3437, 2011.

Fan, X., Xu, Q., Liu, J., Subramanian, S. S., He, C., Zhu, X., and Zhou, L.: Successful early warning and emergency response of a disastrous rockslide in Guizhou province, China, Landslides, 16, 2445–2457, 2019.

Ferretti, A., Prati, C., Rocca, F., Casagli, N., Farina, P., and Young, B.: Permanent Scatterers technology: a powerful state of the art tool for historic and future monitoring of landslides and other terrain instability phenomena, International Conference on Landslide Risk Management, 18th Annual Vancouver Geotechnical Society Symposium, 1–9, 2005.

Ferretti, A., Prati, C., and Rocca, F.: Permanent scatterers in SAR interferometry, IEEE Transactions on geoscience and remote sensing, 39, 8–20, 2001.

Ferretti, A., Fumagalli, A., Novali, F., Prati, C., Rocca, F., and Rucci, A.: A New Algorithm for Processing Interferometric Data-Stacks: SqueeSAR, IEEE Transactions on Geoscience and Remote Sensing, 49, 3460–3470, https://doi.org/10.1109/TGRS.2011.2124465, 2011.

Fiolleau, S., Jongmans, D., Bièvre, G., Chambon, G., Baillet, L., and Vial, B.: Seismic characterization of a clay-block rupture in Harmalière landslide, French Western Alps, Geophys J Int, 221, 1777–1788, 2020.

Fourniadis, I. G., Liu, J. G., and Mason, P. J.: Regional assessment of landslide impact in the Three Gorges area, China, using ASTER data: Wushan-Zigui, Landslides, 4, 267–278, https://doi.org/10.1007/s10346-007-0080-5, 2007.

Guzzetti, F.: Invited perspectives: Landslide populations - Can they be predicted?, Natural Hazards and Earth System Sciences, 21, 1467–1471, https://doi.org/10.5194/nhess-21-1467-2021, 2021.

Handwerger, A. L., Huang, M., Fielding, E. J., Booth, A. M., and Bürgmann, R.: A shift from drought to extreme rainfall drives a stable landslide to catastrophic failure, Sci Rep, 9, 1569, https://doi.org/10.1038/s41598-018-38300-0, 2019.

Handwerger, A. L., Lacroix, P., Bell, A. F., Booth, A. M., Huang, M.-H., Mudd, S. M., Bürgmann, R., and Fielding, E. J.: Multi-sensor remote sensing captures geometry and slow-to-fast sliding transition of the 2017 Mud Creek landslide, Sci Rep, 15, 29831, https://doi.org/10.1038/s41598-025-11399-8, 2025.

Instituto Geofísico del Peru: https://ultimosismo.igp.gob.pe/descargar-datos-sismicos, last access: 1 September 2022.

Intrieri, E., Raspini, F., Fumagalli, A., Lu, P., Del Conte, S., Farina, P., Allievi, J., Ferretti, A., and Casagli, N.: The Maoxian landslide as seen from space: detecting precursors of failure with Sentinel-1 data, Landslides, 15, 123–133, 2018.

Jacquemart, M. and Tiampo, K.: Leveraging time series analysis of radar coherence and normalized difference vegetation index ratios to characterize pre-failure activity of the Mud Creek landslide, California, Natural Hazards and Earth System Sciences, 21, 629–642, https://doi.org/10.5194/nhess-21-629-2021, 2021.

Kumar, V. and Venkataraman, G.: SAR interferometric coherence analysis for snow cover mapping in the western Himalayan region, Int J Digit Earth, 4, 78–90, https://doi.org/10.1080/17538940903521591, 2011.

Lacroix, P., Perfettini, H., Taipe, E., and Guillier, B.: Coseismic and postseismic motion of a landslide: Observations, modeling, and analogy with tectonic faults, Geophys Res Lett, 41, 6676–6680, https://doi.org/10.1002/2014GL061170, 2014.

Lacroix, P., Berthier, E., and Maquerhua, E. T.: Earthquake-driven acceleration of slow-moving landslides in the Colca valley, Peru, detected from Pléiades images, Remote Sens Environ, 165, 148–158, https://doi.org/10.1016/j.rse.2015.05.010, 2015.

Lacroix, P., Bièvre, G., Pathier, E., Kniess, U., and Jongmans, D.: Use of Sentinel-2 images for the detection of precursory motions before landslide failures, Remote Sens Environ, 215, 507–516, https://doi.org/10.1016/j.rse.2018.03.042, 2018.

Lacroix, P., Dehecq, A., and Taipe, E.: Irrigation-triggered landslides in a Peruvian desert caused by modern intensive farming, Nat Geosci, 13, 56–60, 2020.

Lacroix, P., Dini, B., and Cheaib, A.: Measuring Kinematics of Slow-Moving Landslides from Satellite Images, in: Surface Displacement Measurement from Remote Sensing Images, edited by Cavalié O. and Trouvé E., Iste-Wiley, 315–338, https://doi.org/10.1002/9781119986843.ch10, 2022a.

Lacroix, P., Gavillon, T., Bouchant, C., Lavé, J., Mugnier, J.-L., Dhungel, S., and Vernier, F.: SAR and optical images correlation illuminates post-seismic landslide motion after the Mw 7.8 Gorkha earthquake (Nepal), Sci Rep, 12, 6266, 2022b.

Lacroix, P., Huanca, J., Angel, L. A., and Taipe, E.: Precursory Motion and Time-Of-Failure Prediction of the Achoma Landslide, Peru, From High Frequency PlanetScope Satellites, Geophys Res Lett, 50, 1–11, https://doi.org/10.1029/2023GL105413, 2023.

Li, M., Zhang, L., Ding, C., Li, W., Luo, H., Liao, M., and Xu, Q.: Retrieval of historical surface displacements of the Baige landslide from time-series SAR observations for retrospective analysis of the collapse event, Remote Sens Environ, 240, 111695, 2020.

Liu, P., Li, Z., Hoey, T., Kincal, C., Zhang, J., Zeng, Q., and Muller, J.-P.: Using advanced InSAR time series techniques to monitor landslide movements in Badong of the Three Gorges region, China, International Journal of Applied Earth Observation and Geoinformation, 21, 253–264, 2013.

Loew, S., Gschwind, S., Gischig, V., Keller-Signer, A., and Valenti, G.: Monitoring and early warning of the 2012 Preonzo catastrophic rockslope failure, Landslides, 14, 141–154, https://doi.org/10.1007/s10346-016-0701-y, 2017.

López-Quiroz, P., Doin, M.-P., Tupin, F., Briole, P., and Nicolas, J.-M.: Time series analysis of Mexico City subsidence constrained by radar interferometry, J Appl Geophy, 69, 1–15, 2009.

Manconi, A.: How phase aliasing limits systematic space-borne DInSAR monitoring and failure forecast of alpine landslides, Eng Geol, 287, 106094, 2021.

McColl, S. T.: Landslide causes and triggers, in: Landslide Hazards, Risks, and Disasters (Second Edition), edited by: Davies T., Rosser N. and Shroder J.F., Elsevier, 13–41, https://doi.org/10.1016/b978-0-12-818464-6.00011-1, 2022.

Meyer, F. J. and Sandwell, D. T.: SAR interferometry at Venus for topography and change detection, Planet Space Sci, 73, 130–144, https://doi.org/10.1016/j.pss.2012.10.006, 2012.
Notti, D., Meisina, C., Zucca, F., and Colombo, A.: Models to predict Persistent Scatterers data distribution and their capacity to register movement along the slope, Proceedings of FRINGE 2011, 2011, 19–23, 2012.
Palmer, J.: Creeping catastrophes: Studies of slow landslides could unmask the mechanics of a worldwide scourge, Nature, 548, 384–386, https://doi.org/10.1038/548384a, 2017.
Pham, M. Q., Lacroix, P., and Doin, M. P.: Sparsity optimization method for slow-moving landslides detection in satellite image time-series, IEEE Transactions on Geoscience and Remote Sensing, 57, 2133–2144, 2018.
Roy, P., Martha, T. R., Khanna, K., Jain, N., and Kumar, K. V.: Time and path prediction of landslides using InSAR and flow model, Remote Sens Environ, 271, 112899, https://doi.org/10.1016/j.rse.2022.112899, 2022.
Servicio Nacional de Meteorología e Hidrología del Perú: https://www.senamhi.gob.pe/servicios/?p=estaciones, last access: 10 October 2023.
Strozzi, T., Caduff, R., Jones, N., Barboux, C., Delaloye, R., Bodin, X., Kääb, A., Mätzler, E., and Schrott, L.: Monitoring rock glacier kinematics with satellite synthetic aperture radar, Remote Sens (Basel), 12, 1–24, https://doi.org/10.3390/rs12030559, 2020.
Strząbała, K., Ćwiąkała, P., and Puniach, E.: Identification of landslide precursors for early warning of hazards with remote sensing, Remote Sens (Basel), 16, 2781, 2024.
Thollard, F., Clesse, D., Doin, M.-P., Donadieu, J., Durand, P., Grandin, R., Lasserre, C., Laurent, C., Deschamps-Ostanciaux, E., Pathier, E., Pointal, E., Proy, C., and Specht, B.: FLATSIM: The ForM@Ter LArge-Scale Multi-Temporal Sentinel-1 InterferoMetry Service, https://doi.org/10.3390/rs13183734, 2021.
Thouret, J. C., Wörner, G., Gunnell, Y., Singer, B., Zhang, X., and Souriot, T.: Geochronologic and stratigraphic constraints on canyon incision and Miocene uplift of the Central Andes in Peru, Earth Planet Sci Lett, 263, 151–166, https://doi.org/10.1016/j.epsl.2007.07.023, 2007.
Valletta, A., Carri, A., and Segalini, A.: Definition and application of a multi-criteria algorithm to identify landslide acceleration phases, Georisk: Assessment and Management of Risk for Engineered Systems and Geohazards, 16, 555–569, 2022.
Wasowski, J. and Bovenga, F.: Investigating landslides and unstable slopes with satellite Multi Temporal Interferometry: Current issues and future perspectives, Eng Geol, 174, 103–138, 2014.
Wasowski, J. and Bovenga, F.: Remote sensing of landslide motion with emphasis on satellite multi-temporal interferometry applications: an overview, in: Hazards and Disasters Series (Second Edition), edited by: Davies, T., Rosser, N., and Shroder J.F., Elsevier, 365–438, https://doi.org/10.1016/B978-0-12-818464-6.00006-8, 2022.
Van Wyk de Vries, M., Arrell, K., Basyal, G. K., Densmore, A. L., Dunant, A., Harvey, E. L., Jimee, G. K., Kincey, M. E., Li, S., and Singh Pujara, D.: Detection of slow-moving landslides through automated monitoring of surface deformation using Sentinel-2 satellite imagery, Earth Surf Process Landf, 49, 1397–1410, 2024.
Yang, W., Wang, Y., Sun, S., Wang, Y., and Ma, C.: Using Sentinel-2 time series to detect slope movement before the Jinsha River landslide, Landslides, 16, 1313–1324, 2019.
Yang, W., Fang, J., and Liu-Zeng, J.: Landslide-lake outburst floods accelerate downstream slope slippage, Earth Surface Dynamics Discussions, 2021, 1–19, 2021.

Zerathe, S., Lacroix, P., Jongmans, D., Marino, J., Taipe, E., Wathelet, M., Pari, W., Smoll, L. F., Norabuena, E., Guillier, B., and Tatard, L.: Morphology, structure and kinematics of a rainfall controlled slow-moving Andean landslide, Peru, Earth Surf Process Landf, 41, 1477–1493, https://doi.org/10.1002/esp.3913, 2016.

Zhou, C., Yin, K., Cao, Y., Intrieri, E., Ahmed, B., and Catani, F.: Displacement prediction of step-like landslide by applying a novel kernel extreme learning machine method, Landslides, 15, 2211–2225, https://doi.org/10.1007/s10346-018-1022-0, 2018.